Nanoscale

Cite this: *Nanoscale*, 2011, **3**, 2399

www.rsc.org/nanoscale

FEATURE ARTICLE

Tin and germanium monochalcogenide IV–VI semiconductor nanocrystals for use in solar cells

Priscilla D. Antunez, Jannise J. Buckley and Richard L. Brutchey*

Received 22nd January 2011, Accepted 4th March 2011
DOI: 10.1039/c1nr10084j

The incorporation of colloidal semiconductor nanocrystals into the photoabsorbant material of photovoltaic devices may reduce the production costs of solar cells since nanocrystals can be readily synthesized on a large scale and are solution processable. While the lead chalcogenide IV–VI nanocrystals have been widely studied in a variety of photovoltaic devices, concerns over the toxicity of lead have motivated the exploration of less toxic materials. This has led to the exploration of tin and germanium monochalcogenide IV–VI semiconductors, both of which are made up of earth abundant elements and possess properties similar to the lead chalcogenides. This feature article highlights recent efforts made towards achieving synthetic control over nanocrystal size and morphology of the non-lead containing IV–VI monochalcogenides (*i.e.*, SnS, SnSe, SnTe, GeS and GeSe) and their application toward photovoltaic devices.

Introduction

The need for an affordable, secure, and sustainable energy landscape has motivated governments and researchers across disciplines to explore alternative forms of energy, such as solar power. The sun has the potential to supply the world energy demand of *ca.* 363 terawatt hours per day in just seconds, but the high cost of current silicon-based photovoltaics (PVs) has been limiting.[1–3] Consequently, much work has focused on decreasing processing costs through the development of organic- and polymer-based PVs,[4,5] but these devices typically have the disadvantage of a narrow absorption range in addition to poor thermal and environmental stability.[6,7] Other work has focused on colloidal inorganic nanocrystals which share the synthetic advantages of scalability and solution processibility with organic and polymeric materials, but with a potentially wider absorption of the solar spectrum and superior transport properties.[8]

The potential of utilizing colloidal semiconductor nanocrystals in PV devices has led to the development of low-cost processing methods, such as spin-coating,[9,10] ink-jet printing,[11,12] spray coating,[13] and drop casting,[14] at low temperatures and without the need for expensive high vacuum processing methods. Solution-based synthetic methods can now achieve precise control over the nanocrystal size and shape through the manipulation of synthetic variables, such as reaction temperature, reaction time,

Department of Chemistry and the Center for Energy Nanoscience and Technology, University of Southern California, Los Angeles, CA, 90089, USA. E-mail: brutchey@usc.edu

Priscilla D. Antunez

Priscilla D. Antunez received her BS in chemistry from the California State Polytechnic University, Pomona (2009). Since 2009, she has been a graduate student at the University of Southern California in the group of Prof. Richard L. Brutchey. Her research interests include the fabrication of less toxic and more earth abundant nanocrystals for solar cell applications. She was awarded an NSF Graduate Research Fellowship (2010) for her doctoral work.

Jannise J. Buckley

Jannise J. Buckley received her BS in chemistry from the University of California, Santa Cruz (2010). Since 2010, she has been a graduate student at the University of Southern California in the group of Prof. Richard L. Brutchey. Her research interests include elucidating the mechanisms of precursor decomposition and nanocrystal nucleation and growth.

reaction solvent, and the ratio of capping ligand to precursors.[15–25] As a result, the band gap (E_g) of the resulting semiconductor nanocrystal can be tuned through control of the nanocrystal's size and shape below the dimension of its Bohr exciton radius, which ultimately allows for a fine level of control over the energy needed to inject an electron into the conduction band of the material.[26] The lead chalcogenide IV–VI semiconductor nanocrystals (*e.g.*, PbS and PbSe) have been explored as potential earth abundant active layers in PV devices because of the high level of synthetic control that has been achieved in these systems.[27–29]

Lead chalcogenide nanocrystals were the first of the IV–VI class of semiconductor nanocrystals to receive experimental interest as practical PV materials. Beginning in 1985–1986, Nozik and coworkers published the first reports on quantum confinement effects in lead chalcogenides after observing size dependent shifts in the optical absorption spectra of PbS and PbSe nanocrystals.[30,31] The strong quantum confinement effects observed in lead chalcogenides originate from their relatively large Bohr exciton radii, which range from 20 nm for PbS to 46 nm for PbSe.[32] Comparatively, other II–VI and III–V classes of semiconductors (*e.g.*, CdTe and GaAs) have smaller Bohr exciton radii that are <15 nm.[32] An important consequence of the large Bohr exciton radii is the ability to tailor band gap energies of the lead chalcogenides; for example, the band gap of PbSe can be tuned from 1.2–0.5 eV by increasing the nanocrystal diameter from 2–15 nm, respectively.[33] The ease of size tunability on the nanoscale becomes specifically useful in device design. Consequently, lead chalcogenide nanocrystals with controlled size and morphology have been incorporated into to a variety of PV devices.

In 2008, Nozik *et al.* prepared an all-inorganic lead chalcogenide/aluminium Schottky junction solar cell based on colloidally synthesized nanocrystal thin films.[34] It was found that the most efficient devices resulted from thin films of PbSe nanocrystals that were 4 nm in diameter (E_g = 0.9 eV). The PbSe-based device was fabricated from ITO/PbSe/Al layers which gave large short-circuit photocurrents (J_{SC} = 24.5 mA cm^{-2}), low open-circuit voltages (V_{OC} = 239 mV), modest fill factors (FF = 0.41) and a spectrally corrected AM1.5G power conversion efficiency of η_P = 2.1%. The devices did not require sintering or superlattice ordering for charge carrier transport; however, the device was highly air sensitive and light absorption was hindered by thin active layers required by the placement of the Schottky junction at the back contact. Although device architectures based on Schottky junctions show promise for solar energy conversion, they are typically limited by low open circuit voltages. In order to mitigate these limitations, alternative device architectures such as p–n or p–i–n junctions may be necessary. Moreover, third generation solar cells that might take advantage of multiple exciton generation (MEG) in lead chalcogenide nanocrystals may be another way to improve device efficiencies past current values through the generation of two or more excitons from a single incident photon.[35–37]

Despite the extremely promising results obtained thus far for lead chalcogenide-based PVs, the toxicity of lead and the potential of lead exposure are considered a significant threat to public health.[38,39] Lead is a poisonous substance known to affect most systems in the body, including the production of red blood cells, the kidneys, and the central nervous system.[40,41] Recent studies have even shown adverse effects (such as intellectual deficits) in children with low bloodstream lead levels (BLLs < 10 μg dL^{-1}).[42] In response to lead's adverse physiological effects, the European Food Safety Authority (EFSA) has recently decreased the tolerable exposure level to 0.50 μg kg^{-1} bodyweight per day.[43] The decreasing threshold for BLLs observed over the past 20–30 years underscores the importance of exploring alternative semiconductor materials that are less toxic, but have otherwise similar properties to the lead chalcogenides. Tin(II) and germanium(II) monochalcogenides are less toxic than the lead chalcogenides; and unlike lead, inorganic tin compounds are not readily absorbed into the bloodstream through ingestion or inhalation.[44] Although studies have cautioned over excessive exposure to germanium,[45] the toxicity of most germanium compounds is considered low.[46] The tin and germanium monochalcogenides are made up of earth abundant elements,[47] and posses many other properties similar to the lead chalcogenides, which make them particularly attractive targets as the photoabsorbant material in nanocrystal-based PVs.

While the tin and germanium monochalcogenides (*i.e.*, SnS, SnSe, SnTe, GeS, and GeSe) appear to be promising replacements for the lead chalcogenides in PV applications, the number of reports of tin and germanium monochalcogenide nanocrystals in the literature over the past decade remains relatively small. Moreover, the same degree of synthetic control over size and morphology that has been achieved in the lead chalcogenides has not yet been realized in these related systems. This feature article highlights the recent work by our group and others on the synthesis of high quality tin and germanium monochalcogenide nanocrystals and their application towards PV devices. It will be seen that while the degree of synthetic control over these systems is approaching that of the lead chalcogenides, their application toward nanocrystal-based PV devices still remains limited, albeit with a great deal of potential promise.

Richard L. Brutchey

Prof. Richard L. Brutchey received his BS in chemistry from the University of California, Irvine (2000) and his PhD in chemistry from the University of California, Berkeley (2005) with Prof. T. Don Tilley. After a post-doctoral fellowship with Prof. Daniel E. Morse at the University of California, Santa Barbara, he began his independent career in 2007 at the University of Southern California where he is currently an Assistant Professor of Chemistry. The Brutchey group focuses on the design of rational synthetic routes to inorganic nanostructures for use in solar energy conversion, energy storage, and catalysis. Prof. Brutchey was named a Cottrell Scholar by the Research Corporation for Science Advancement (2010) for his work on less toxic and more earth abundant absorber materials for use in solar cells.

General structural characteristics of tin and germanium monochalcogenides

The germanium and tin chalcogenides possess rather unique optical and electronic properties resulting from the diverse compositions and structures of these materials. An example of this diversity can be seen in the family of tin monochalcogenides where both layered 2-D (*e.g.*, SnS and SnSe) and 3-D (*e.g.*, SnTe) crystal structures are observed. This rich structural chemistry is partially a result of the Sn^{2+} oxidation state in these materials (*vide infra*), and can be further complicated by the ability of tin to access the Sn^{4+} oxidation state and possess coordination numbers in the solid state ranging between 2 and 9.[48,49]

The two most common crystal structures observed in germanium and tin monochalcogenide IV–VI semiconductors are the cubic NaCl (rock salt) and the orthorhombic GeS structures. In bulk, the sulfides and selenides (*i.e.*, GeS, GeSe, SnS, and SnSe) possess an orthorhombic *Pnma* structure at low temperatures.[49,50] This structure is best described as a highly distorted rock salt structure that is comprised of zig-zag double layer planes of the metal monochalcogenide separated by a van der Waals gap of *ca.* 1 Å (Fig. 1). The local arrangement about the Sn^{2+} or Ge^{2+} cations is that of a distorted octahedron (coordination number = 6). In this structure, the cation–anion bond angles deviate slightly from 90°, and there are three short and three long bonds about the cation. This distortion can be primarily attributed to the Sn(5s) and Ge(4s) lone pairs for Sn^{2+} and Ge^{2+}, respectively (Fig. 2).[51,52] The strong anisotropic properties observed in SnS and SnSe, for example, have been correlated to this double layer structure, and it has been observed that the electrical conductivity and Hall mobility at room temperature are five to six times higher when measured along the layers instead of along the crystallographic *c* axis.[53]

Tin sulfide (SnS) occurs naturally as herzenbergite in rare mineral form. At room temperature, the thermodynamically preferred phase is that of α-SnS (a = 11.14 Å, b = 3.97 Å, and c = 4.34 Å). Above 600 °C, the *Pnma* structure converts into the orthorhombic *Cmcm* β-SnS structure (a = 4.12 Å, b = 11.48 Å, and c = 4.17 Å).[54] In addition, there is a known metastable phase of SnS (a = 6.00 Å) that possesses a cubic structure.[55] Similarly, the thermodynamically preferred phase of α-SnSe is the orthorhombic *Pnma* structure (a = 11.50 Å, b = 4.15 Å, and c = 4.45 Å), which undergoes a phase transition at *ca.* 523 °C to the orthorhombic *Cmcm* β-SnSe structure (a = 4.31 Å, b = 11.70 Å, and c = 4.31 Å).[54,56] At room temperature, β-SnTe possesses a cubic *Fm3m* structure (a = 6.32 Å), similar to the lead monochalcogenides, that is stable up to 727 °C at which point a congruent melt occurs.[57] Solid-state studies have shown a low temperature cubic β-SnTe to rhombohedral α-SnTe phase transition occurs at *ca.* −200 °C.[54]

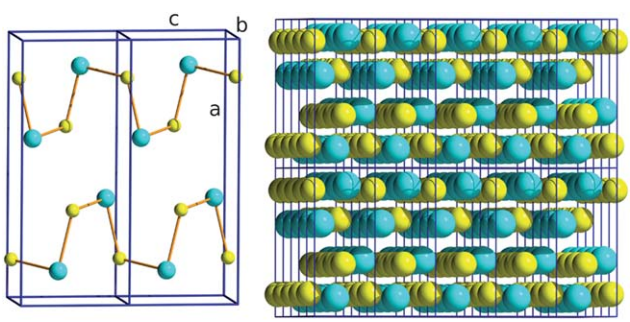

Fig. 1 The GeS structure. The yellow shaded atoms represent sulfur while the aquamarine shaded atoms represent germanium.

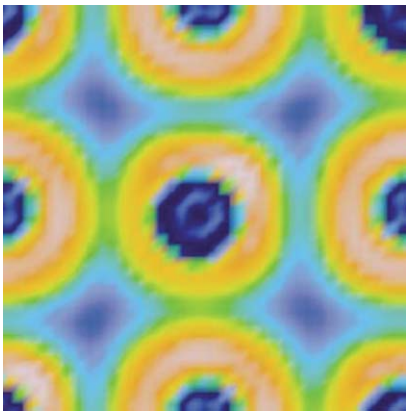

Fig. 2 Calculated valence electron localization function for a distorted GeS structure. Lighter colors signify regions of strong electron localization, while darker colors signify poorly localized regions. The Ge(4s) lone pair is observed as an area of high electron localization at the top right of the center cation. Reprinted with permission from ref. 64 (Copyright 2003 American Physical Society).

The thermodynamically preferred phase of GeS at room temperature is that of the orthorhombic *Pnma* α-GeS structure (a = 10.47 Å, b = 3.64 Å, and c = 4.30 Å). Above 600 °C, the orthorhombic *Pnma* structure undergoes a phase transition to the hexagonal β-GeS structure (a = 8.70 Å, c = 8.73 Å).[58] Similarly, the thermodynamically preferred phase of GeSe at room temperature is also an orthorhombic *Pnma* α-GeSe structure (a = 4.40 Å, b = 3.85 Å, and c = 10.82 Å).[59] This phase undergoes a phase transition at *ca.* 586 °C to the cubic *Fm3m* β-GeSe structure (a = 5.73 Å).[60]

The tin monochalcogenides possess an electron configuration of $4d^{10}5s^25p^0$ for Sn^{2+}; where the two Sn(5p) electrons are involved in bond formation, and the two Sn(5s) electrons act as a lone pair.[49] The electron configuration for the corresponding chalcogenide anion is ns^2np^6. The band structure for SnS and SnSe is such that the main contribution to the top of the valence band is from the p orbitals of S^{2-} or Se^{2-} (with some degree of hybridization with the cation *s* band), while the main contribution to the bottom of the conduction band is from the empty p orbitals of Sn^{2+}.[49,61–64] The Sn(5s) lone pair does not participate in bonding to a great extent, but leads to a distortion from octahedral geometry about the Sn^{2+} cations (*vide supra*). Tight binding calculations predict that the direct band gap decreases down the group for bulk tin monochalcogenides (E_g = 2.1 eV for SnS, 1.3 eV for SnSe and 1.1 eV for SnTe). Moreover, it has been calculated that both bulk SnS and SnSe possess indirect band gaps that are close in energy to the direct band gaps (E_g = 1.5 eV for SnS and 0.9 eV for SnSe).[49] Similar to the tin monochalcogenides, GeS and GeSe also possess closely placed direct and indirect band gaps (E_g = 1.6–1.7 eV for GeS and E_g = 1.1–1.2 eV for GeSe) that overlap well with the solar spectrum.[65,66]

Nanocrystal synthesis and characterization

Tin sulfide nanocrystals

The bulk properties of SnS have been studied extensively and it has been found that the material is stable under ambient conditions. Consistent with its layered crystal structure (*vide supra*), SnS is an anisotropic native p-type semiconductor with reported hole mobilities on the order of 90 $cm^2 V^{-1} s^{-1}$ perpendicular to its *c* axis at 27 °C.[67,68] As a result of its bulk transport properties and high absorption coefficient of *ca.* 10^4 cm^{-1}, SnS has promise as an absorber in PV devices.[69,70]

In an effort to explore the properties of SnS on the nanoscale, several solvothermal methods have produced 0-D spherical particles, 1-D whiskers, and even 3-D tetrahedral nano- and microcrystals.[71–76] In 2006, Greyson *et al.* synthesized SnS nano- and microcrystals with a metastable zinc blende crystal structure which differs from the thermodynamically preferred orthorhombic phase.[76] The SnS nano- and microcrystals were prepared by the reaction of $SnCl_2$ with elemental sulfur at 170 °C in oleylamine. Scanning electron microscopy (SEM) images showed tetrahedral nano- and microcrystals ranging between 200 and 300 nm on each side (Fig. 3a). Modifications in the reaction time or amine surfactant (decyl-, dodecyl-, hexadecyl-, and oleylamine) did not have an effect on the size, polydispersity, or shape of the SnS product. The metastable zinc blende crystal structure ($a = 5.85$ Å) was verified by powder X-ray diffraction (XRD); however, small amounts of Sn, sulfur, $Sn(OH)_2$ and orthorhombic SnS were also observed (Fig. 3b). Up to this point, the zinc blende phase had only been observed in bulk SnS grown epitaxially on a NaCl seed layer.[77,78] Selected-area electron diffraction (SAED) confirmed that the SnS nano- and microcrystals were single crystalline; while a lattice spacing of $d = 8.1 \pm 0.2$ Å was observed for the (110) lattice fringes by high-resolution transmission electron microscopy (TEM). Greyson *et al.* also explored the thermal stability of their as-synthesized SnS by heating the nano- and microcrystals under Ar at 300 °C for 3 h, and observed no change in the SnS morphology or crystal structure. In contrast, when the SnS nano- and microcrystals were heated in the presence of oleylamine at 250 °C for 3 h, a nearly complete conversion (>90%) from zinc blende to orthorhombic platelets was observed. This phase transformation in solution may be a result of the oleylamine lowering the activation barrier for structural rearrangement.

The orthorhombic SnS platelets possessed a similar absorption profile to that of bulk orthorhombic SnS, with a strong absorption onset at *ca.* 980 nm (corresponding to the direct band gap at $E_g = 1.3$ eV) and a weaker absorption edge near 1100 nm (corresponding to the indirect band gap at $E_g = 1.1$ eV). The calculated band structure of zinc blende SnS predicts that the material is either a metal or a small indirect band gap semiconductor; however, the absorption profile of the zinc blende tetrahedra is blue shifted to 700 nm ($E_g = 1.8$ eV) relative to the orthorhombic phase. The higher energy band gap for the zinc blende phase relative to the orthorhombic phase may be a result of the different symmetries of the crystal structures; however, the impurities observed by XRD in the zinc blende SnS may also play a role in the spectral blue shift.

In 2008, Hickey *et al.* synthesized monodisperse and slightly sulfur-rich sub-10 nm SnS nanocrystals with a narrow 10% size distribution (Fig. 4).[79] The SnS nanocrystals were synthesized by the hot injection of thioacetamide in oleylamine into a mixture of $Sn[N(SiMe_3)_2]_2$, oleic acid, trioctylphosphine, and octadecene at 170 °C. Variation of the oleic acid/oleylamine ratio allowed for shape control. A 1 : 2 ratio of oleic acid/oleylamine produced spherical nanocrystals, whereas a 1 : 1 ratio produced faceted nanocrystals with a distinct triangular or truncated triangular projection. Between these two extremes, the nanocrystals were found to be monodisperse, but their morphology was difficult to define. It was also found that as the concentration of oleic acid

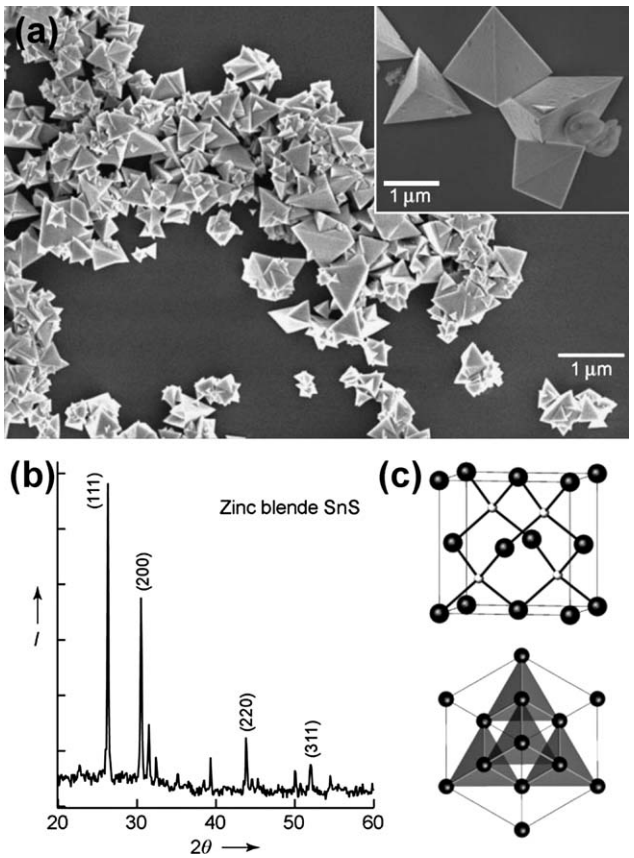

Fig. 3 (a) SEM images of zinc blende SnS microcrystals synthesized from $SnCl_2$ and elemental sulfur. (b) XRD pattern of the zinc blende SnS. (c) Cubic unit cell of zinc blende SnS viewed off the (100) axis (top) and down the (111) axis (bottom). Reprinted with permission from ref. 76 (Copyright 2006 Wiley-VCH).

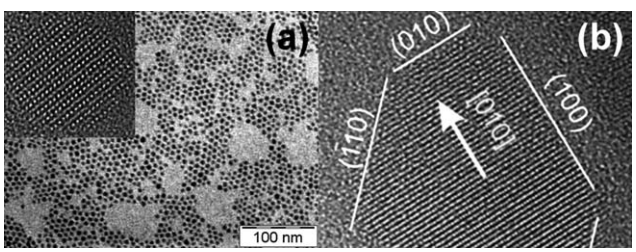

Fig. 4 (a) TEM images of spherical SnS nanocrystals synthesized from $Sn[N(SiMe_3)_2]_2$ and thioacetamide. (b) High-resolution TEM image of a single SnS nanocrystal. Reprinted with permission from ref. 79 (Copyright 2008 American Chemical Society).

increased, the nanocrystals became larger in size. The authors determined that other Sn^{2+} precursors, such as $Sn(OAc)_2$ and Sn $(oleate)_2$, produced material with a large sheet-like morphology rather than small monodisperse nanocrystals.

The nanocrystals were found to possess the orthorhombic α-SnS crystal structure ($a = 4.31$ Å, $b = 11.26$ Å, $c = 3.98$ Å) typical of these materials; however, a small number of peaks attributed to the zinc blende phase and surface-oxidized SnO were also observed by XRD. The absorption profile of clear solutions of the spherical SnS nanocrystals was very steep and blue shifted as compared to bulk SnS, with a calculated indirect band gap of $E_g = 1.6$ eV. While the bulk material possesses both direct and indirect band gaps that are relatively close in energy (*i.e.*, 200–600 meV), the authors suggest that the positions of these two band gaps relative to one another may change as a function of quantum confinement. The applicability of these SnS nanocrystals as a photoconductive material was assessed through a photoelectrochemical experiment whereby a thin film of the nanocrystals was irradiated with 470 nm light and the photocurrent was measured (Fig. 5). It was found that the photocurrent response for the SnS nanocrystals was stable and repeatable over many light/dark cycles.

In 2009, Xu *et al.* synthesized sub-5 nm SnS nanocrystals that were dispersible in polar solvents, such as ethanol.[80] In this method, $SnBr_2$ was reacted with Na_2S in ethylene glycol at room temperature in the presence of various stabilizing ethanolamines as ligands. Three different ethanolamines were used as stabilizing ligands: triethanolamine (TEA), *N*-methyldiethanolamine (MDEA), or *N*,*N*-dimethylethanolamine (DMEA). Among the three ethanolamines surveyed, TEA (with three hydroxyl groups) produced the smallest and most monodisperse SnS nanocrystals. It is thought that TEA plays dual roles of (1) coordinating to the Sn^{2+} to form a $[Sn(TEA)_n]^{2+}$ precursor complex, and (2) strongly binding to the SnS nanocrystal surface upon nucleation through the multiple hydroxyl groups. As the number of hydroxyl groups decrease in the ethanolamines, the resulting nanocrystals gradually get larger and less monodisperse with TEA yielding nanocrystals of 3.2 ± 0.5 nm, MDEA yielding nanocrystals of 4.0 $\pm$ 2.0 nm, and DMEA yielding nanocrystals of 5.0 ± 4.0 nm in diameter.

The highly crystalline nature of the SnS nanocrystals was demonstrated by observation of atomic lattice fringes by HR-TEM for apparent single-crystalline particles. SAED was used to confirm that the nanocrystals were in the expected orthorhombic α-SnS phase ($a = 11.14$ Å, $b = 3.97$ Å, and $c = 4.34$ Å), with no other phases being observed. Transmission spectra on colloidal 5.0 nm SnS nanocrystal dispersions indicated an indirect band gap at $E_g = 1.1$ eV that is similar to the bulk, and no fluorescence was observed for these SnS nanocrystals, which may be consistent with their indirect band gap behavior.

In 2010, Liu *et al.* synthesized SnS nanocrystals that were single crystalline, monodisperse, and size-tunable (Fig. 6).[81] The nanocrystals were synthesized by the hot injection of $S(SiMe_3)_2$ in octadecene into a solution of $SnCl_2$ in oleylamine at 200 °C. After the addition of oleic acid, the SnS nanocrystals remained dispersed in toluene for more than 6 months if stored under an inert atmosphere. Nanocrystal size can be controlled between 6, 12, and 20 nm by varying injection and growth temperatures between 120, 150, and 210 °C, respectively. It was also determined that a 1 h incubation yielded monodisperse SnS nanocrystals, while a 5 min incubation yielded a larger size distribution suggesting a size-focusing growth mechanism.

The resulting nanocrystals were found to be in the orthorhombic β-SnS phase ($a = 4.14$ Å, $b = 11.49$ Å, $c = 4.17$ Å), as determined by XRD analysis. No band gap shift was observed between the three differently sized samples (6, 12, and 20 nm), which all showed an absorption onset at *ca.* 1.55 eV similar to that reported by Hickey *et al.*;[79] however, Liu *et al.* assigned it to a direct band gap transition rather than an indirect band gap transition.

Most recently, Ning *et al.* reported the synthesis of SnS nanostructures with various sizes and morphologies.[82] In this preparation, $Sn_6O_4(OH)_4$ was used as the Sn^{2+} precursor. The $Sn_6O_4(OH)_4$ precursor was dissolved in oleic acid and oleylamine, and then thioacetamide was injected with oleylamine at elevated temperatures ranging from 120–150 °C. If the

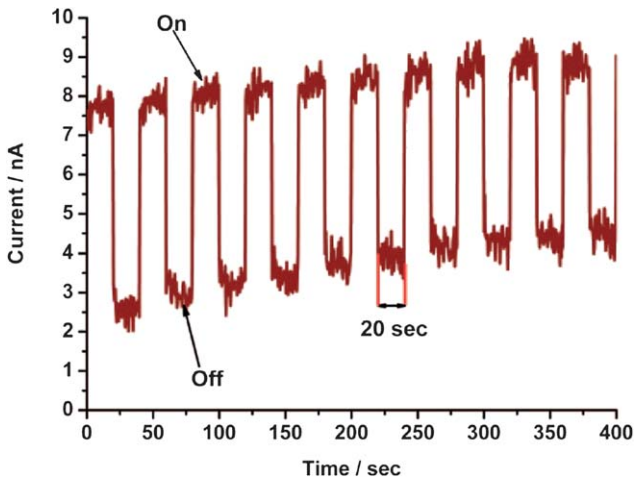

Fig. 5 Photocurrent response of a thin film of SnS nanocrystals on an ITO substrate in 0.1 M sodium sulfate electrolyte ($E_{app} = 800$ mV *vs.* Ag/AgCl). Reprinted with permission from ref. 79 (Copyright 2008 American Chemical Society).

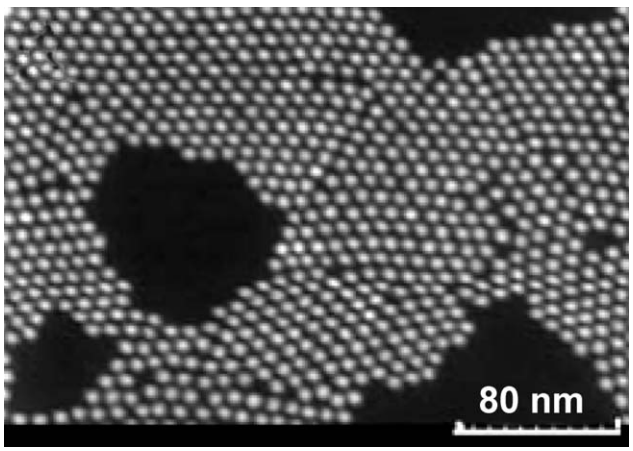

Fig. 6 SEM image of 6 nm SnS nanocrystals synthesized from $SnCl_2$ and $S(SiMe_3)_2$. Reprinted with permission from ref. 81 (Copyright 2010 IOP Publishing).

thioacetamide was injected at 150 °C with a 1 : 1 molar ratio of Sn/S, then 5 nm SnS nanocrystals were produced. If the thioacetamide was injected at 120 °C with a 2 : 1 molar ratio of Sn/S, then 13 nm, single-crystalline SnS nanoflowers were produced through oriented attachment. As the reaction time was increased from 3–10 min, the SnS nanoflowers converted to amorphous SnS with a sheet-like morphology. The authors do not discuss whether the nanocrystals are in the expected 1 : 1 stoichiometry for SnS, or if varying the Sn/S ratio makes the resulting nanocrystals either sulfur- or tin-rich.

XRD analysis of the nanocrystals and nanoflowers confirmed they were in the expected orthorhombic α-SnS crystal structure ($a = 4.33$ Å, $b = 11.19$ Å, and $c = 3.98$ Å). Absorption spectra of the 5 nm SnS nanocrystals suggest both indirect and direct optical band gaps of $E_g = 1.6$ and 3.6 eV, respectively. Emission spectra produced by excitation between 340 and 380 nm appear to confirm the direct band gap in SnS with an emission maximum at 3.2–3.6 eV. Both the indirect and direct band gaps are blue shifted as a result of quantum confinement effects; however, the direct wide band gap is blue shifted substantially more than that of the indirect band gap from bulk values.

Tin selenide nanocrystals

Similar to SnS, SnSe has also proven to be a promising lead-free IV–VI PV material.[83] Bulk SnSe exhibits p-type conductivity, with hole mobilities up to 10^3 cm^2 V^{-1} s^{-1} along the c axis at −196 °C.[84,85] The indirect and direct band gaps ($E_g = 0.90$ eV and 1.30 eV, respectively) of bulk SnSe correlate well with the optimum band gap values for solar cells, which fall between $E_g = 1.0$ and 1.5 eV.[49] In 2007, Pejova and Grozdanov demonstrated the effects of quantum confinement in SnSe by studying the optical properties of SnSe nanocrystals deposited as a thin film with an average grain size of 14.8 nm.[86] The as-deposited nanocrystals possessed indirect and direct band gaps of $E_g = 1.20$ and 1.74 eV, respectively, which are both blue shifted from the band gaps of the bulk material. This suggests that the nanocrystalline grains were smaller than the Bohr exciton radius for SnSe. Upon annealing the films to 150 °C for 1 h, the average grain size increased to 23.3 nm, accompanied by a red shift of the indirect and direct band gaps to $E_g = 1.10$ and 1.65 eV, respectively. Promptly after demonstrating quantum confinement effects in nanocrystalline SnSe thin films, Pejova and Tanusevski went on to demonstrate the potential of SnSe as an active component in PVs by studying the charge-transport properties of these films.[87] Their findings showed that SnSe is a photoconductive material with contributions from both indirect and direct band transitions that are close in energy, which agrees with previous work.[49] The dominant charge carriers are holes, indicating that the SnSe semiconductor films are p-type and act as acceptors when in a solar cell device. Thermionic emission over the crystal grain boundaries was determined to be the predominant charge transport mechanism at room temperature. The average lifetime of the minority charge carriers (electrons) was relatively high (1.78 ms), giving further favorable evidence for using SnSe thin films as absorber materials in solar cells.

A number of solution-phase synthetic routes to SnSe nanocrystals have been reported over the past decade; however, many of these reports lacked the synthetic control needed to produce well-defined nanocrystals.[88–91] In 1999, Wang *et al.* reported a mild, low temperature reductive route to ill-defined and morphologically diverse SnSe nanorods (approximate dimensions 30 nm × 1.5 μm) using an ethylenediamine chelate to direct growth.[88] In 2000, Zhang *et al.* published an aqueous route to nanocrystalline SnSe with large, sheet-like morphologies.[89] The product precipitated immediately upon the reaction of a highly alkaline aqueous solution of selenium and a mixture of $SnCl_2$ with tartaric acid. It is possible that the absence of structure-directing ligands other than the tartrate present in the alkaline mixture led to the large, ill-defined nanocrystalline product. In 2003, Shen *et al.* synthesized the first SnSe nanowires with high aspect ratios (*i.e.*, ∼150) and a narrow size distribution.[90] They used a simple, rapid ethylenediamine-assisted polyol process at 200 °C with selenium and $SnCl_2$. They believe the ethylenediamine was the key factor to obtain phase pure SnSe nanowires because it reduces the elemental selenium to form Se^{2-}. The morphology of the SnSe product is also highly dependent on the presence of ethylenediamine. Without the addition of ethylenediamine, the SnSe product was found to contain unreacted elemental selenium and showed flake and particle morphology. They believe ethylenediamine forms a precursor $[Sn(en)_2]^{2+}$ complex that serves as a molecular template whereby selenium ions may coordinate to form one-dimensional SnSe nanorod structures; however, a high degree of particulate product is still observed with the introduction of ethylenediamine. In 2004, Han *et al.* reported the room temperature preparation of SnSe nanorods in a similar route to Zhang *et al.*[89,91] Nanorods of SnSe were produced by mixing a highly alkaline aqueous selenium solution with $SnCl_2$ in the presence of trisodium citrate. The agglomerated nanorods had an average diameter of 90 nm and lengths up to 1 μm. As with the Zhang synthesis, the highly alkaline conditions (>10 M NaOH) needed to completely dissolve the Se make the synthesis method less than ideal.

In 2002, Schlecht *et al.* took a different approach to the solution-phase SnSe synthesis by employing diorganodichalcogenides as soluble chalcogenide sources.[92] They turned to diphenyl diselenide (Ph_2Se_2) because of its solubility in diglyme, after they were unable to obtain nanocrystalline SnSe by directly reacting Sn^0 with elemental selenium. The overall reaction required two-steps. In the first step, 2 equiv of Ph_2Se_2 reacted with activated tin at 65 °C in THF to produce a $Sn(SePh)_4$ selenolate rather than the intended SnSe.

In the second step, thermolysis of $Sn(SePh)_4$ at 300 °C leads to the formation of nanocrystalline SnSe with byproducts of Ph_2Se and Ph_2Se_2. The resulting nanocrystals possessed a broad size distribution (3–50 nm) with no control over particle morphology.

Recent advancements in the solution-phase synthesis of well-defined SnSe nanocrystals were made by Franzman *et al.* in 2010 with the first publication of small colloidal SnSe nanocrystals shown to exhibit quantum confinement effects.[93] Their synthetic route involved the use of a diorganodichalcogenide as the chalcogen source.[94–99] A stoichiometric amount of di-*tert*-butyl diselenide ($^tBu_2Se_2$) was injected into a solution of anhydrous $SnCl_2$, dodecylamine, and dodecanethiol at 95 °C. Following injection, the reaction temperature was raised to 180 °C for 4 min and then quenched by cooling to obtain phase-pure SnSe nanocrystals. They found that control over the nanocrystal composition, and more specifically the oxidation state of tin, could easily be

obtained by controlling the amount of $^{t}Bu_2Se_2$ added to the reaction. Addition of 0.5 equiv of the $^{t}Bu_2Se_2$ gives phase pure SnSe, while addition of 1.0 equiv of the $^{t}Bu_2Se_2$ gives $SnSe_2$ in a result similar to Schlecht *et al.*[92]

Transmission electron microscopy analysis revealed the SnSe product to be composed of elongated anisotropic nanocrystals of variable length and consistent width (19.0 nm ± 5.1 nm; Fig. 7). The product was phase pure and crystallized in the typical orthorhombic phase (a = 11.55 Å, b = 4.16 Å, c = 4.45 Å) with a distorted rock salt structure. A 48 : 52 tin to selenium ratio, with Sn^{2+} and Se^{2-} oxidation states, was confirmed through a combination of energy-dispersive X-ray spectroscopy (EDX) and X-ray photoelectron spectroscopy (XPS). The SnSe nanocrystals absorbed through the visible spectrum and into the near-IR having a direct band gap (E_g = 1.71 eV) which was blue-shifted relative to the bulk (E_g = 1.30 eV) due to quantum confinement effects. Given the potential of these quantum confined SnSe nanocrystals, their utility in a hybrid PV device was explored (*vide infra*).

The size, shape, and surface chemistry of quantum confined SnSe nanocrystals were further investigated by Baumgardner *et al.*[100] They successfully carried out a solution-phase synthesis of SnSe through hot (65–175 °C) injection of $Sn[N(SiMe_3)_2]_2$ into TOPSe in the presence of oleylamine. After nucleation, oleic acid was introduced to the mixture and then the reaction was quenched. The resulting SnSe nanocrystals were unagglomerated and quasispherical in shape, as revealed by TEM analysis. It was observed that the SnSe nanocrystal shape is sensitive to the surface ligands present. When oleic acid was present prior to precursor injection, nucleation was inhibited. This finding differs from previous PbSe/Te syntheses, where oleic acid was used to tune the nucleation step.[20,101] For the SnSe synthesis, Baumgardner *et al.* attributed the inhibition of nucleation with oleic acid to the high binding affinity of oleate for Sn^{2+}, and the resulting lowered chemical potential driving force for nucleation. When oleic acid was injected after nucleation, it was found that growth was accelerated until the equilibrium size was reached. Replacing oleic acid with dodecanethiol resulted in the growth of anisotropic SnSe nanocrystals, similar to those produced by Franzman *et al.*[93]

With this synthetic method, SnSe nanocrystals from 4 to 10 nm could be controllably synthesized by tuning the injection and reaction temperatures (Fig. 8), and manipulation of the reaction temperature was also found to affect the crystal structure. Reaction temperatures held at 175 °C produced α-SnSe nanocrystals exhibiting the *Pnma* crystal structure; however, when the reaction temperature was lowered to 105 °C, a decrease of the nanocrystal diameter was observed with a concomitant increase in the *d*-spacings of several reflections. The observed increase in *d*-spacing suggests that the SnSe crystal structure changed from *Pnma* to *Cmcm* symmetry, which is typically only observed after high temperature annealing of bulk SnSe to 600 °C. The formation of β-SnSe nanocrystals with the *Cmcm* crystal structure is further supported by the disappearance of the characteristic *Pnma* (020) and (112) reflections in the XRD pattern. This is an interesting result because a metastable phase is being observed at lower temperatures.[54,56,102,103]

Nanocrystals in the size range from 4–9 nm exhibited quantum confinement effects, similar to the results observed by Franzman *et al.* The indirect band gap varied from E_g = 1.2–0.9 eV for nanocrystal sizes ranging from 4–9 nm (Fig. 9a), respectively, while the direct band gap varied from E_g = 1.8–1.3 eV over the

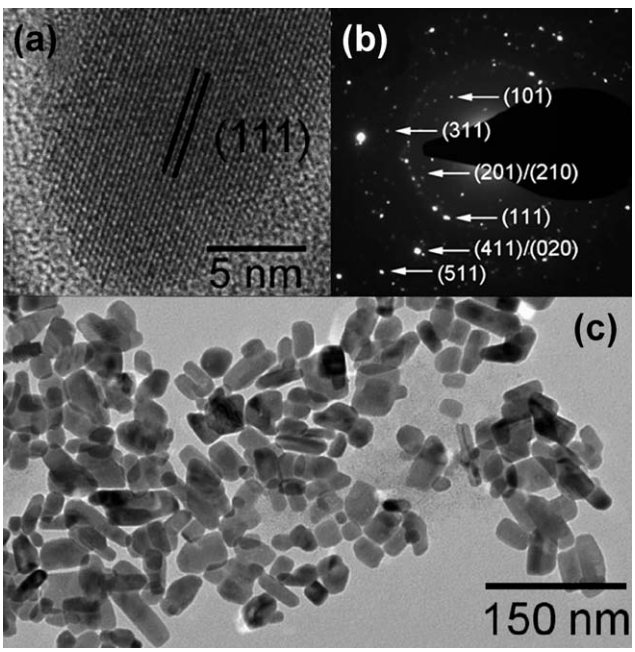

Fig. 7 TEM images of SnSe nanocrystals synthesized from $SnCl_2$ and $^{t}Bu_2Se_2$. (a) High-resolution TEM image of a single nanocrystal. (b) SAED pattern for an ensemble of SnSe nanocrystals. (c) Low-resolution TEM image of SnSe nanocrystals. Reprinted with permission from ref. 93 (Copyright 2010 American Chemical Society).

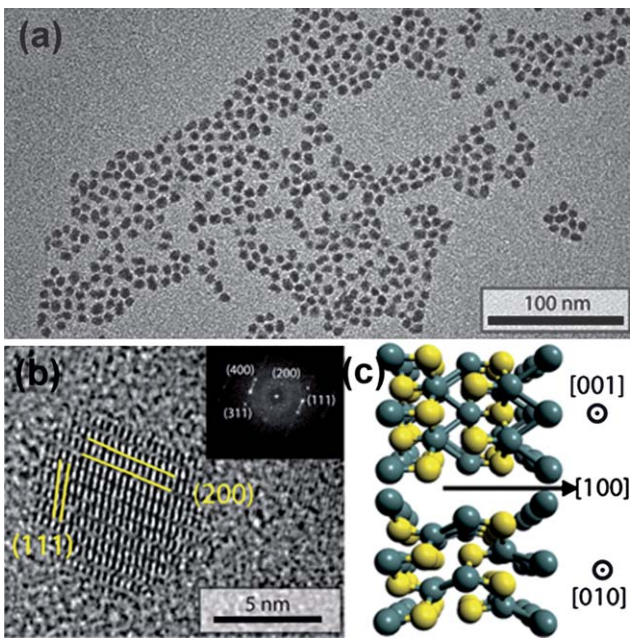

Fig. 8 (a) Low-resolution TEM image of SnSe nanocrystals synthesized from $Sn[N(SiMe_3)_2]_2$ and TOPSe. (b) High-resolution TEM image of a single nanocrystal. (c) The (001) and (010) projections of a SnSe unit cell with *Pnma* symmetry. Reprinted with permission from ref. 100 (Copyright 2010 American Chemical Society).

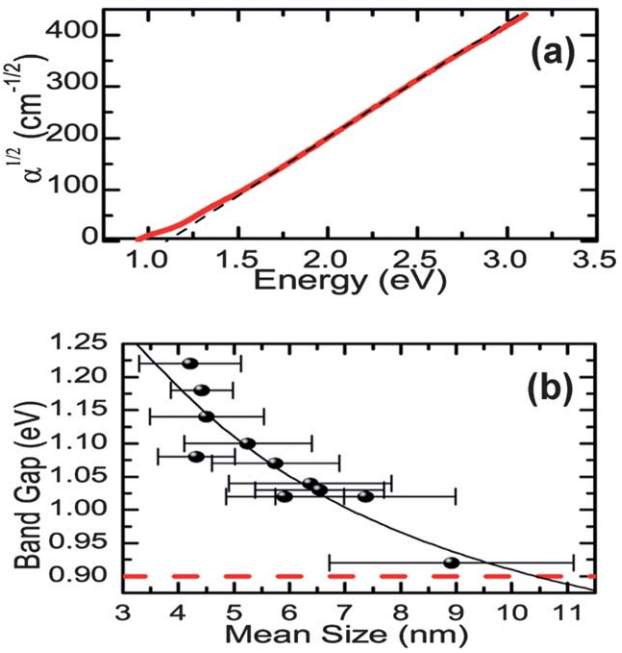

Fig. 9 (a) Tauc plot from UV-vis-NIR data for SnSe nanocrystals showing an indirect band gap. (b) Approximate $1/r^2$ relationship between band gap and mean nanocrystal size. Reprinted with permission from ref. 100 (Copyright 2010 American Chemical Society).

same size range. Both the indirect and direct band gaps demonstrated a rough $1/r^2$ dependence on the nanocrystal size (Fig. 9b). Although a prototype solar cell was not reported, the Hanrath group did report the applicability of their SnSe nanocrystals as a photoconductive material. The photoconductivity of formic acid passivated SnSe films over interdigitated gold electrodes was confirmed through transient current–voltage (I–V) characteristics. Transient photocurrent was observed at a bias of 2 V μm^{-1} under 100 mW cm^{-2} illumination; however, significant signal degradation occurred over time. This photocurrent degradation was attributed to the photooxidation of organic species (*i.e.*, formic acid or oleic acid) bound to the nanocrystal surface.

Tin telluride nanocrystals

Narrow band gap IV–VI semiconductor nanocrystals can be used for NIR-absorbing PV devices (*e.g.*, in a tandem cell); however, it has been a challenge to synthesize nanocrystals with band gap energies below 0.5 eV.[104,105] Bulk SnTe is isotropic, which allows for relatively high p-type conductivity with hole mobilities of 840 $cm^2\ V^{-1}\ s^{-1}$ at 27 °C.[106] Tin telluride is a direct band gap semiconductor that exhibits a narrow band gap of $E_g =$ 0.2 eV at room temperature,[107] and the observation of quantum-size effects in SnTe nanocrystals by Kovalenko *et al.* has sparked interest in this material as a stable and less toxic semiconductor in PV applications.[108]

One of the first solvothermal syntheses of tin monochalcogenides entailed the use of soluble diaryl dichalcogenides and activated Sn^0 nanocrystals.[92] This work evolved from the use of elemental selenium and tellurium to the use of diphenyl diselenide (Ph_2Se_2) and ditelluride (Ph_2Te_2) to obtain single-phase SnSe and SnTe micro- and nanocrystals. All syntheses began with the known reduction method of $SnCl_2$ by $Li[Et_3BH]$ in THF and diglyme to produce the Sn^0 nanocrystal precursor.[109] The reaction of Sn^0 with Ph_2Te_2 produced two different morphologies of the crystalline material. Concentrated reaction mixtures produced large 60 nm agglomerates with random orientation; but as the reaction concentration decreased, smaller 15 × 40 nm star-shaped nanocrystals were formed. The cubic rock-salt structure (a = 6.33 Å) of the SnTe nanocrystals was determined by HRTEM, SAED and XRD to closely match that of the bulk SnTe, and the 1 : 1 stoichiometry of Sn : Te was confirmed by EDX. As discussed previously, the equivalent reaction with Ph_2Se_2 yielded the discrete selenolate $Sn(SePh)_4$, and a short pyrolysis at 300 °C was needed to convert the product into SnSe nanocrystals.

In 2007, Kovalenko *et al.* synthesized monodisperse SnTe nanocrystals in solution that were tunable in size between 4.5 and 15 nm (Fig. 10), with their corresponding band gaps ranging between $E_g = 0.8$ and 0.38 eV, respectively.[108] The stoichiometric SnTe nanocrystals were prepared by the reaction of $Sn[N(SiMe_3)_2]_2$ in octadecene with TOPTe in oleylamine at 150 °C, with oleic acid being added to passivate the surface of the resulting nanocrystals. The uniform and nearly spherical shape of the nanocrystals is evident from the TEM analysis, while the cubic rock-salt crystal structure (a = 6.24 Å) was confirmed by XRD and HRTEM. Increasing the concentration of oleylamine and the temperature of injection/incubation generally resulted in larger SnTe nanocrystals.

The absorption spectra of the SnTe nanocrystals were studied to determine the size effect on the optical band gap. The resulting nanocrystals possessed broad excitonic peaks in the IR region that blue-shifted with decreasing size, consistent with quantum confinement effects. The optical band gaps for the 14 and 7.2 nm SnTe nanocrystals were $E_g = 0.54$ and 0.39 eV, respectively; these values are near the calculated optimal value of 0.35 eV for semiconductors that may exhibit MEG.[110] The charge transport properties of thin films of the SnTe nanocrystals were studied to evaluate their potential in PV and thermoelectric applications. The resulting low electrical conductivities of $\sigma \approx 10^{-10}$ S cm^{-1} were likely the result of the large interparticle spacing in the films,

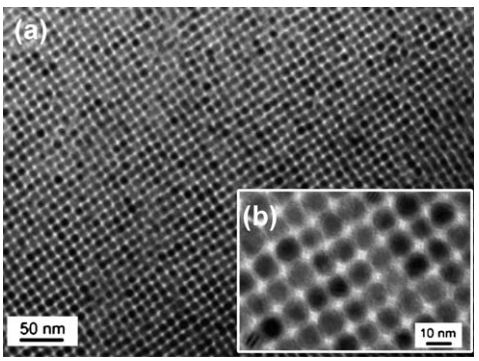

Fig. 10 (a and b) TEM images of 10 nm SnTe nanocrystals synthesized from $Sn[N(SiMe_3)_2]_2$ and TOPTe. Reprinted with permission from ref. 108 (Copyright 2007 American Chemical Society).

but the conductivity increased by almost six orders of magnitude when the films were treated with hydrazine in anhydrous acetonitrile (Fig. 11). The hydrazine treated films showed n-type conductivity, indicated by the increase in conductivity when a positive bias was applied to the back gate electrode.

More recently, Ning *et al.* were able to synthesize SnTe nanocrystals and nanowires.[111] The unique properties exhibited by nanorods and nanowires make these low dimensional materials attractive,[112] and have motivated studies on their formation *via* aggregation of 0-D nanocrystals by oriented attachment.[113] The synthesis of the SnTe nanocrystals was achieved by the hot injection of TOPTe into a mixture of $Sn_6O_4(OH)_4$, oleic acid, and oleylamine (or octylamine) at 180 °C. The product was incubated at 165 °C, and formed stable concentrated colloidal solutions upon purification. Transmission electron microscopy images confirm that when oleylamine is used, the resulting SnTe nanocrystals were *ca.* 4 nm in diameter. When the oleylamine was replaced by shorter octylamine ligands, the resulting nanocrystals were larger (~8 nm) in size and of low crystallinity; however, these nanocrystals transformed into 50 nm long crystalline nanowires at extended reaction times through oriented attachment. The authors speculate that the shorter chain amine induced a faster growth rate of the nanocrystals that in turn caused a larger size and lower crystallinity when compared to the longer chain oleylamine.[114] The crystalline SnTe nanowires grew along the (100) direction, and at extended reaction times, the SnTe nanowires reached 150 nm in length and 10 nm in width.

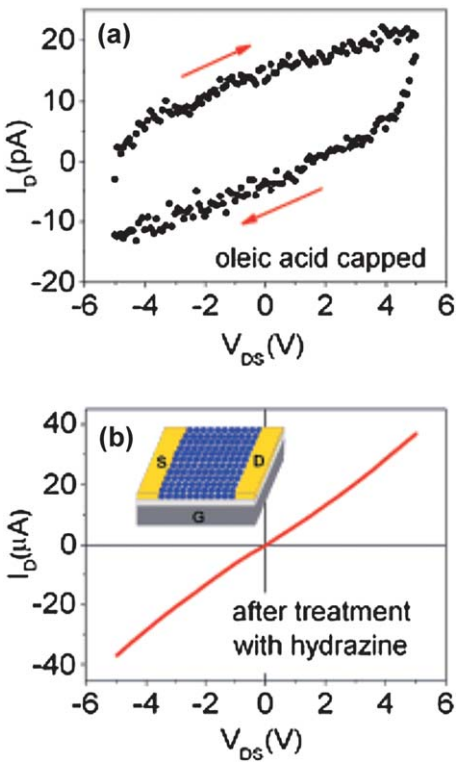

Fig. 11 *I–V* curves for films of the (a) oleic acid capped (b) hydrazine treated SnTe nanocrystals. Upon treatment with hydrazine, the SnTe nanocrystals demonstrate n-type behavior. Reprinted with permission from ref. 108 (Copyright 2007 American Chemical Society).

Germanium sulfide and selenide nanocrystals

Similar to the tin analogs, both bulk GeS and GeSe are native p-type semiconductors; for example, hole mobilities of 90 $cm^2 V^{-1} s^{-1}$ have been measured along the *c* axis for GeS at 27 °C.[115,116] Vaughn *et al.* have recently reported the first solution chemistry route for colloidal GeS and GeSe nanostructures.[117] The complicated band structure and the closeness of the direct and indirect band gaps of GeS and GeSe result in a range of values for both the direct and indirect band gaps (E_g = 1.6–1.7 eV for GeS and E_g = 1.1–1.2 eV for GeSe) that overlap well with the solar spectrum.[65,66] The GeS nanosheets were synthesized *via* the reduction of GeI_4 in hexamethyldisilazane, oleylamine, oleic acid, and dodecanethiol at 320 °C for 24 h. To synthesize GeSe nanosheets, TOPSe was used as the selenium precursor in place of dodecanethiol. TEM images show mainly elongated hexagons (2–4 μm by 0.5–1 μm; Fig. 12), with thicknesses between 3 and 20 nm for GeS and 5–100 nm for GeSe (as estimated by AFM). The phase-pure orthorhombic GeS and GeSe nanosheets are both oriented along the [100] direction. The lattice parameters for GeS (a = 10.52 Å, b = 3.65 Å, and c = 4.30 Å) and GeSe (a = 10.78 Å, b = 3.81 Å, and c = 4.37 Å) corresponded well with literature values.

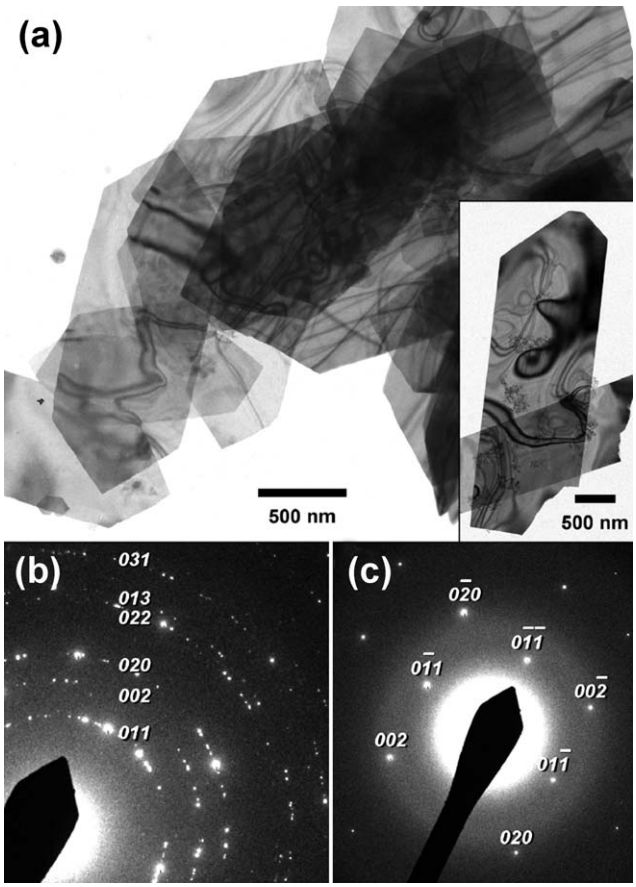

Fig. 12 (a) TEM images of GeS and GeSe (inset) nanosheets synthesized from GeI_4 and dodecanthiol or TOPSe, respectively. SAED patterns for (b) an ensemble of GeS nanosheets and (c) a single crystalline GeS nanosheet oriented along the [100] direction. Reprinted with permission from ref. 117 (Copyright 2010 American Chemical Society).

Diffuse reflectance spectroscopy was used to approximate the indirect and direct band gaps of GeS (E_g = 1.58 and 1.61 eV, respectively) and GeSe (E_g = 1.14 and 1.21 eV, respectively), which are very close to the values of the bulk band gap. Four-point *I–V* measurements were used to measure a conductivity of $\sigma = 4.7 \times 10^{-6}$ S cm^{-1} for drop-cast thin films of the GeSe nanosheets, while a two-point *I–V* measurements demonstrate the p-type character of this material (Fig. 13). The conductivity value is comparable to other colloidal nanocrystalline semiconductor thin films.[118]

Photovoltaic device applications

Recent advancements in the development of simple, reproducible and low-cost synthetic techniques towards high-quality tin and germanium monochalcogenide nanocrystals have led to the end goal of their inclusion into thin film PV device architectures. To date, the reported devices remain limited to the inclusion of either SnS or SnSe nanocrystals into various device architectures; however, the data appear promising thus far. For example, Stavrinadis *et al.* showed that inclusion of SnS nanocrystals into a lead chalcogenide type II bilayer heterojunction solar cell resulted in larger open-circuit voltages (V_{OC} = 0.44 V) as compared to Schottky cells based on pure PbSe or PbS nanocrystals.[119] In this work, SnS nanocrystals were incorporated into an ITO/SnS/PbS/Al device stack. The open-circuit voltage was >100% larger than that of the control Schottky ITO/PbS/Al device (V_{OC} = 0.20 V). They attributed the increase in open circuit voltage of the device to the built-in electric field of the SnS/PbS heterojunction, which acts as an electron blocking layer that assists in the diffusion of charge carriers to their respective contacts. The short-circuit current, fill factor and overall power conversion efficiencies (J_{SC} = 1.84 mA cm^{-2}, FF = 0.30, η_P = 0.31%) of the bilayer device were generally found to be lower than other reported lead chalcogenide Schottky devices.[34] They believe the key to future optimization (*i.e.*, increasing J_{SC}) lies in improving the synthesis and post-synthesis processing techniques of the nanocrystals; however, their results do suggest that SnS nanocrystalline films can lead to substantially improved properties of multilayer PVs.

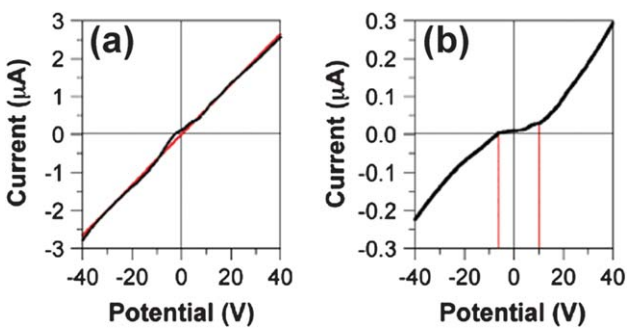

Fig. 13 (a) Four-point *I–V* curve giving a conductivity of $s = 4.7 \times 10^{-6}$ S cm^{-1} for dropcast films of the GeSe nanosheets. (b) Two-point *I–V* curve giving turn-on potentials of −6.5 and +10 V suggesting p-type character for the GeSe nanosheets. Reprinted with permission from ref. 117 (Copyright 2010 American Chemical Society).

Wang *et al.* showed that the addition of SnS nanocrystals into hybrid polymer containing bulk heterojunction PV cells improves the device performance when compared to pristine polymer devices lacking the SnS.[120] Their device was structured as ITO/PEDOT:PSS/SnS:polymer/Al, where the active layer was synthesized by blending the nanocrystals with poly[2-methoxy-5-(3′,7′-dimethyloctyloxy)-1,4-phenylenevinylene] (MDMO-PPV) or poly(3-hexylthiophene) (P3HT). Both active layers gave improvements in the absorption intensity and range of the absorption spectrum upon incorporation of the SnS nanocrystals. The power conversion efficiency ($\eta_P = 1.08 \times 10^{-2}$%) of the SnS:P3HT solar cells was highest at 86 wt% SnS, due to an increased short-circuit density (J_{SC} = 0.026 mA cm^{-2} *vs.* 0.017 mA cm^{-2} for neat polymer); however, this came at the cost of V_{OC} and fill factor due to changes in P3HT morphology upon addition of SnS. The performance of the SnS:MDMO-PPV active layer showed greater improvements in power conversion efficiency upon addition of SnS nanocrystals, specifically at 67 wt % SnS ($\eta_P = 2.05 \times 10^{-2}$%), without the decreases in V_{OC} and fill factor observed for P3HT cells. At 67 wt% SnS in MDMO-PPV, the power conversion efficiency was 26.6 times that of neat polymer cell.

More recently, Wang *et al.* showed improvement by one order of magnitude on the power conversion efficiency of their previously reported SnS:MDMO-PPV PV cell by using SnS/SnO heterojunction nanocrystals rather than pure SnS nanocrystals.[121] The improved performance of this device is a result of the unique SnS/SnO rod-like morphology (as compared to the 0-D SnS morphology), which allows for more facile charge transport within the inorganic phase and improved current density in the device. Moreover, the addition of SnO into the inorganic phase widens the band gap and, as a result, V_{OC} increases from 0.37 V for the SnS:MDMO-PPV device to 0.74 V for the SnS/SnO:MDMO-PPV device.

The first demonstration of PV application of a cell based on TiO_2/SnS films was reported in 2010 by Wang *et al.*[122] An electrochemical solar cell structure of FTO/Pt + electrolyte + SnS/TiO_2/FTO yielded a high V_{OC} = 0.471 V, a J_{SC} = 0.30 mA cm^{-2}, a power conversion efficiency of η_P = 0.10%, and FF = 0.71 under 1 sun illumination. Power conversion efficiencies dropped to η_P = 0.03% without the presence of the nanocrystalline SnS layer, proving that addition of the SnS results in better PV performance. The authors mention that this SnS/TiO_2 device compares favorably with previously published CIS/In_2S_3/TiO_2 device architectures.[123]

Tin selenide nanocrystals have also recently been used as PV materials in hybrid polymer/nanocrystal device architectures. In 2010, Franzman *et al.* demonstrated the utility of SnSe nanocrystals by integrating them into a conducting polymer as the electron accepting layer in a hybrid PV device.[93] Their device consisted of a SnSe:poly[2-methoxy-5-(3′,7′-dimethyloctyloxy)-1,4-phenylenevinylene] (MDMO-PPV) absorbing layer, a perylene-3,4,9,10-tetracarboxylic diimide (PTCDI) acceptor/hole-blocking layer, and a LiF/Al bilayer cathode on a glass substrate. When compared to analogous neat polymer devices, it was found that the J_{SC} of the SnSe hybrid cell was nearly twice that of the neat MDMO-PPV cell. Both the V_{OC} and fill factors of the two were comparable suggesting the absence of charge trapping on the SnSe nanocrystals. The power conversion

efficiency was improved by 100% ($\eta_P = 0.03\%$ for neat MDMO-PPV compared to $\eta_P = 0.06\%$ for SnSe/MDMO-PPV) upon inclusion of SnSe into the polymer (0.25 : 1.0, w/w, SnSe/MDMO-PPV). The external quantum efficiency doubled near 500 nm with the absorption coefficient remaining nearly the same at that wavelength for the hybrid device compared to the neat polymer. These data indicate that the polymer acts as the primary absorber and the observed increase in power conversion efficiency is likely a result of electron transfer from MDMO-PPV to the SnSe nanocrystals. It should be noted that this was the first reported synthesis and utilization of quantum confined SnSe nanocrystals in a PV device, and that much improvement is still needed in order for this material to function as an earth abundant absorber material.

Conclusions

A variety of tin and germanium monochalcogenide nanocrystals have been synthesized over the past decade. The majority of these syntheses utilize a hot-injection type approach whereby a chalcogenide source (*e.g.*, trioctylphosphine chalcogenide, diorganodichalcogenide, thio/selenocarbonyl, dissolved elemental source, *etc.*) is injected into a hot solution of the metal precursor (*e.g.*, metal salt, metal amide, dissolved metal oxo cluster, *etc.*) and various stabilizing ligands. These methods have yielded nanocrystals of various sizes and shapes, with varying degrees of quality in terms of monodispersity, morphological fidelity, and phase purity. The first major challenge in this chemistry results from the tendency of the GeS, GeSe, SnS and SnSe nanocrystals to form sheet-like structures (similar to those synthesized by Vaughn *et al.*) instead of 0-D particles. This morphological effect is a direct result of the *Pnma* double layer crystal structure that these materials adopt, as opposed to the rock salt structure adopted by SnTe and the lead chalcogenides. The second major challenge in this chemistry is the synthesis of phase pure nanocrystals, since metastable phases can be easily accessed, in addition to the crystalline impurities that result from oxidation of tin and germanium to the Sn^{4+} and Ge^{4+} oxidation states. While a great deal of progress has been achieved in overcoming these challenges, the same level of size control and monodispersity that has been realized in the lead chalcogenides has still not been achieved in these systems. Moreover, there has not been much success in controlling the dimensionality of a given tin or germanium monochalcogenide nanocrystal between 0-D, 1-D, 2-D and 3-D type structures.

While there have been some notable reports of using SnS in heterojunction solar cells (*e.g.*, $\eta_P = 1.3\%$ for a SnO_2/SnS/CdS/In device structure[69]), the majority of PV devices derived from SnS or SnSe nanocrystals have thus far demonstrated rather poor power conversion efficiencies ($\eta_P < 1\%$). The single greatest challenge in increasing the performance of these PV devices is to achieve a greater degree of control over the SnS and SnSe nanocrystal surface. Significant device improvements will be made by removing the insulating ligands protecting the nanocrystals and replacing them with small molecules, such as hydrazine or metal chalcogenide clusters.[124,125] This will allow for much improved interparticle coupling (*i.e.*, charge transport through the polycrystalline layer), which is a function of interparticle spacing and nanocrystal surface chemistry.[118] Moreover, if MEG is demonstrated in low band gap non-lead containing IV–VI semiconductor nanocrystals (such as SnTe), this would also represent a major advancement with regards to these materials and their potential applications in PV devices.

Acknowledgements

We thank the Center for Energy Nanoscience, an Energy Frontier Research Center funded by the US Department of Energy, Office of Science, Office of Basic Energy Sciences, under Award DE-SC0001013 for funding. Portions of this work, and financial support for J. J. B., were funded by the National Science Foundation under DMR-0906745. P. D. A. acknowledges the National Science Foundation for a Graduate Research Fellowship and R. L. B. acknowledges the Research Corporation for Science Advancement for a Cottrell Scholar Award.

References

1 C. E. Schoder, *Futurist*, 2011, **45**, 25.
2 N. S. Lewis, *Science*, 2007, **315**, 798.
3 N. S. Lewis and D. G. Nocera, *Proc. Natl. Acad. Sci. U. S. A.*, 2006, **103**, 15729.
4 K. M. Coakley and M. D. McGehee, *Chem. Mater.*, 2004, **16**, 4533.
5 J. Y. Kim, K. Lee, N. E. Coates, D. Moses, T. Q. Nguyen, M. Dante and A. J. Heeger, *Science*, 2007, **317**, 222.
6 S. E. Shaheen, D. S. Ginley and G. E. Jabbour, *MRS Bull.*, 2005, **30**, 10.
7 M. C. Scharber, D. Wuhlbacher, M. Koppe, P. Denk, C. Waldauf, A. J. Heeger and C. L. Brabec, *Adv. Mater.*, 2006, **18**, 789.
8 E. H. Sargent, *Nat. Photonics*, 2009, **3**, 325.
9 I. Gur, N. A. Fromer, M. L. Geier and A. P. Alivisatos, *Science*, 2005, **310**, 462.
10 Y. Wu, C. Wadia, W. Ma, B. Sadtler and A. P. Alivisatos, *Nano Lett.*, 2008, **8**, 2551.
11 H. M. Haverinen, R. A. Myllyla and G. E. Jabbour, *Appl. Phys. Lett.*, 2009, **94**, 073108.
12 M. Singh, H. M. Haverinen, P. Dhagat and G. E. Jabbour, *Adv. Mater.*, 2010, **22**, 673.
13 V. A. Akhavan, B. W. Goodfellow, M. G. Panthani, D. K. Reid, D. J. Hellebusch, T. Adachi and B. A. Korgel, *Energy Environ. Sci.*, 2010, **3**, 1600.
14 J. Tang, G. Konstantatos, S. Hinds, S. Myrskog, A. G. Pattantyus-Abraham, J. Clifford and E. H. Sargent, *ACS Nano*, 2009, **3**, 331.
15 W. G. Lu, J. Y. Fang, K. L. Stokes and J. Lin, *J. Am. Chem. Soc.*, 2004, **126**, 11798.
16 J. E. Murphy, M. C. Beard, A. G. Norman, S. P. Ahrenkiel, J. C. Johnson, P. R. Yu, O. I. Micic, R. J. Ellingson and A. J. Nozik, *J. Am. Chem. Soc.*, 2006, **128**, 3241.
17 C. B. Murray, S. H. Sun, W. Gaschler, H. Doyle, T. A. Betley and C. R. Kagan, *IBM J. Res. Dev.*, 2001, **45**, 47.
18 K. S. Cho, D. V. Talapin, W. Gaschler and C. B. Murray, *J. Am. Chem. Soc.*, 2005, **127**, 7140.
19 W. G. Lu, J. Y. Fang, Y. Ding and Z. L. Wang, *J. Phys. Chem. B*, 2005, **109**, 19219.
20 E. Lifshitz, M. Bashouti, V. Kloper, A. Kigel, M. S. Eisen and S. Berger, *Nano Lett.*, 2003, **3**, 857.
21 C. B. Murray, D. J. Norris and M. G. Bawendi, *J. Am. Chem. Soc.*, 1993, **115**, 8706.
22 W. W. Yu, J. C. Falkner, B. S. Shih and V. L. Colvin, *Chem. Mater.*, 2004, **16**, 3318.
23 C. M. Evans, L. Guo, J. J. Peterson, S. Maccagnano-Zacher and T. D. Krauss, *Nano Lett.*, 2008, **8**, 2896.
24 L. Cademartiri, J. Bertolotti, R. Sapienza, D. S. Wiersma, G. von Freymann and G. A. Ozin, *J. Phys. Chem. B*, 2006, **110**, 671.
25 X. Peng, *Adv. Mater.*, 2003, **15**, 459.
26 M. G. Bawendi, M. L. Steigerwald and L. E. Brus, *Annu. Rev. Phys. Chem.*, 1990, **41**, 477.
27 A. J. Nozik, *Nano Lett.*, 2010, **10**, 2735.

28 A. J. Nozik, M. C. Beard, J. M. Luther, M. Law, R. J. Ellingson and J. C. Johnson, *Chem. Rev.*, 2010, **110**, 6873.
29 A. Luque, A. Marti and A. J. Nozik, *MRS Bull.*, 2007, **32**, 236.
30 J. M. Nedeljkovic, M. T. Nenadovic, O. I. Micic and A. J. Nozik, *J. Phys. Chem.*, 1986, **90**, 12.
31 A. J. Nozik, F. Williams, M. T. Nenadovic, T. Rajh and O. I. Micic, *J. Phys. Chem.*, 1985, **89**, 397.
32 F. W. Wise, *Acc. Chem. Res.*, 2000, **33**, 773.
33 A. Lipovskii, E. Kolobkova, V. Petrikov, I. Kang, A. Olkhovets, T. Krauss, M. Thomas, J. Silcox, F. Wise, Q. Shen and S. Kycia, *Appl. Phys. Lett.*, 1997, **71**, 3406.
34 J. M. Luther, M. Law, M. C. Beard, Q. Song, M. O. Reese, R. J. Ellingson and A. J. Nozik, *Nano Lett.*, 2008, **8**, 3488.
35 R. J. Ellingson, M. C. Beard, J. C. Johnson, P. Yu, O. I. Micic, A. J. Nozik, A. Shabaev and A. L. Efros, *Nano Lett.*, 2005, **5**, 865.
36 J. M. Luther, M. C. Beard, Q. Song, M. Law, R. J. Ellingson and A. J. Nozik, *Nano Lett.*, 2007, **7**, 1779.
37 A. J. Nozik, *Chem. Phys. Lett.*, 2008, **457**, 3.
38 R. R. Jones, *Lancet*, 1989, **2**, 669.
39 L. Sharmer, M. S. Shackley and A. K. Harding, *J. Environ. Health*, 2010, **73**, 8.
40 N. C. Papanikolaou, E. G. Hatzidaki, S. Belivanis, G. N. Tzanakakis and A. M. Tsatsakis, *Med. Sci. Monit.*, 2005, **11**, 329.
41 R. R. Dietert, J. E. Lee, I. Hussain and M. Piepenbrink, *Toxicol. Appl. Pharmacol.*, 2004, **198**, 86.
42 B. P. Lanphear, R. Hornung, J. Khoury, K. Yolton, P. Baghurst, D. C. Bellinger, R. L. Canfield, K. N. Dietrich, R. Bornschein, T. Greene, S. J. Rothenberg, H. L. Needleman, L. Schnaas, G. Wasserman, J. Graziano and R. Roberts, *Environ. Health Perspect.*, 2005, **113**, 894.
43 P. Grandjean, *Lancet*, 2010, **376**, 855.
44 *Toxicology Desk Reference: The Toxic Exposure and Medical Monitoring Index*, ed. R. P. Ryan and C. E. Terry, Taylor and Francis, Philadelphia, 1999, ISBN 1-56032-795-2.
45 B. Swennen, A. Mallants, H. Roels, J. P. Buchet, A. Bernard, R. R. Lauwerys and D. Lison, *Occup. Environ. Med.*, 2000, **57**, 242.
46 G. B. Gerber and A. Leonard, *Mutat. Res.*, 1997, **387**, 141.
47 US Geological Survey, *Rare Earth Elements—Critical Resources for High Technology*, http://pubs.usgs.gov/fs/2002/fs087-02, accessed January 2011.
48 T. Jiang and G. A. Ozin, *J. Mater. Chem.*, 1998, **8**, 1099.
49 I. Lefebvre, M. A. Szymanski, J. Oliver-Fourcade and J. C. Jumas, *Phys. Rev. B: Condens. Matter Mater. Phys.*, 1998, **58**, 1896.
50 J. M. Chamberlain and M. Merdan, *J. Phys. C: Solid State Phys.*, 1977, **10**, L571.
51 I. Lefebvre, M. Lannoo, G. Allan, A. Ibanez, J. Fourcade, J. C. Jumas and E. Beaurepaire, *Phys. Rev. Lett.*, 1987, **59**, 2471.
52 I. Lefebvre, M. Lannoo, J. Olivier-Fourcade and J. C. Jumas, *Phys. Rev. B: Condens. Matter Mater. Phys.*, 1991, **44**, 1004.
53 W. Albers, C. Haas and F. Vandermaesen, *J. Phys. Chem. Solids*, 1960, **15**, 306.
54 A. A. Volykhov, V. I. Shtanov and L. V. Yashina, *Inorg. Mater.*, 2008, **44**, 345.
55 A. N. Mariano and K. L. Chopra, *Appl. Phys. Lett.*, 1967, **10**, 282.
56 H. Wiedemeier and F. J. Csillag, *Z. Kristallogr.*, 1979, **149**, 17.
57 S. S. Kabalkina, N. R. Serebryanaya and L. F. Vereshchagin, *Sov. Phys. Solid State*, 1968, **10**, 574.
58 G. Bissert and K. F. Hesse, *Acta Crystallogr., Sect. B: Struct. Crystallogr. Cryst. Chem.*, 1978, **34**, 1322.
59 S. N. Dutta and G. A. Jeffrey, *Inorg. Chem.*, 1965, **4**, 1363.
60 H. Wiedemeier and P. A. Siemers, *Z. Anorg. Allg. Chem.*, 1975, **411**, 90.
61 R. Car, G. Ciucci and L. Quartapelle, *Phys. Status Solidi B*, 1978, **86**, 471.
62 N. S. Dantas, A. F. da Silva and C. Persson, *Opt. Mater.*, 2008, **30**, 1451.
63 A. Walsh and G. W. Watson, *Phys. Rev. B: Condens. Matter Mater. Phys.*, 2004, **70**, 235114.
64 U. V. Waghmare, N. A. Spaldin, H. C. Kandpal and R. Seshadri, *Phys. Rev. B: Condens. Matter Mater. Phys.*, 2003, **67**, 125111.
65 L. Makinistian and E. A. Albanesi, *J. Phys.: Condens. Matter*, 2007, **19**, 186211.
66 L. Makinistian and E. A. Albanesi, *Phys. Rev. B: Condens. Matter Mater. Phys.*, 2006, **74**, 045206.
67 J. B. Johnson, H. Jones, B. S. Latham, J. D. Parker, R. D. Engelken and C. Barber, *Semicond. Sci. Technol.*, 1999, **14**, 501.
68 W. Albers, C. Haas, H. J. Vink and J. D. Wasscher, *J. Appl. Phys.*, 1961, **32**, 2220.
69 K. T. R. Reddy, N. K. Reddy and R. W. Miles, *Sol. Energy Mater. Sol. Cells*, 2006, **90**, 3041.
70 H. Noguchi, A. Setiyadi, H. Tanamura, T. Nagatomo and O. Omoto, *Sol. Energy Mater. Sol. Cells*, 1994, **35**, 3256.
71 S. K. Panda, S. Gorai and S. Chaudhuri, *Mater. Sci. Eng., B*, 2006, **129**, 265.
72 S. K. Panda, A. Datta, A. Dev, S. Gorai and S. Chaudhuri, *Cryst. Growth Des.*, 2006, **6**, 2177.
73 M. Salavati-Niasari, D. Ghanbari and F. Davar, *J. Alloys Compd.*, 2010, **492**, 570.
74 S. Schlecht and L. Kienle, *Inorg. Chem.*, 2001, **40**, 5719.
75 D. S. Koktysh, J. R. McBride and S. J. Rosenthal, *Nanoscale Res. Lett.*, 2007, **2**, 144.
76 E. C. Greyson, J. E. Barton and T. W. Odom, *Small*, 2006, **2**, 368.
77 S. B. Badachhape and A. Goswami, *J. Phys. Soc. Jpn.*, 1962, **17**, 251.
78 A. N. Mariano and K. L. Chopra, *Appl. Phys. Lett.*, 1967, **10**, 282.
79 S. G. Hickey, C. Waurisch, B. Rellinghaus and A. Eychmüller, *J. Am. Chem. Soc.*, 2008, **130**, 14978.
80 Y. Xu, N. Al-Salim, C. W. Bumby and R. D. Tilley, *J. Am. Chem. Soc.*, 2009, **131**, 15990.
81 H. T. Liu, Y. Liu, Z. Wang and P. He, *Nanotechnology*, 2010, **21**, 105707.
82 J. J. Ning, K. K. Men, G. J. Xiao, L. Wang, Q. Q. Dai, B. Zou, B. B. Liu and G. T. Zou, *Nanoscale*, 2010, **2**, 1699.
83 Z. Zainal, S. Nagalingam, A. Kassim, M. Z. Hussein and W. M. M. Yunus, *Sol. Energy Mater. Sol. Cells*, 2004, **81**, 261.
84 H. Maier and D. R. Daniel, *J. Electron. Mater.*, 1977, **6**, 693.
85 J. Umeda, *J. Phys. Soc. Jpn.*, 1961, **16**, 124.
86 B. Pejova and I. Grozdanov, *Thin Solid Films*, 2007, **515**, 5203.
87 B. Pejova and A. Tanusevski, *J. Phys. Chem. C*, 2008, **112**, 3525.
88 W. Wang, Y. Geng, P. Yan, F. Lui, Y. Xie and Y. Qian, *J. Am. Chem. Soc.*, 1999, **121**, 4062.
89 W. X. Zhang, Z. H. Yang, J. W. Liu, L. Zhang, Z. H. Hui, W. C. Yu, Y. T. Qian, L. Chen and X. M. Liu, *J. Cryst. Growth*, 2000, **217**, 157.
90 G. Z. Shen, D. Chen, X. Jiang, K. B. Tang, Y. K. Lui and Y. T. Qian, *Chem. Lett.*, 2003, **32**, 426.
91 Q. Han, Y. Zhu, X. Wang and W. Ding, *J. Mater. Sci.*, 2004, **39**, 4643.
92 S. Schlecht, M. Budde and L. Kienle, *Inorg. Chem.*, 2002, **41**, 6001.
93 M. A. Franzman, C. W. Schlenker, M. E. Thompson and R. L. Brutchey, *J. Am. Chem. Soc.*, 2010, **132**, 4060.
94 D. H. Webber and R. L. Brutchey, *Inorg. Chem.*, 2011, **50**, 723.
95 M. E. Norako and R. L. Brutchey, *Chem. Mater.*, 2010, **22**, 1613.
96 M. E. Norako, M. A. Franzman and R. L. Brutchey, *Chem. Mater.*, 2009, **21**, 4299.
97 D. H. Webber and R. L. Brutchey, *Chem. Commun.*, 2009, 5701.
98 M. A. Franzman and R. L. Brutchey, *Chem. Mater.*, 2009, **21**, 1790.
99 M. A. Franzman, V. Perez and R. L. Brutchey, *J. Phys. Chem. C*, 2009, **113**, 630.
100 W. J. Baumgardner, J. J. Choi, Y. F. Lim and T. Hanrath, *J. Am. Chem. Soc.*, 2010, **132**, 9519.
101 J. J. Urban, D. V. Talapin, E. V. Shevchenko and C. B. Murray, *J. Am. Chem. Soc.*, 2006, **128**, 3248.
102 A. C. Bernardes-Silva, A. F. Mesquita, E. D. Neto, A. O. Porto, J. D. Ardisson, G. M. de Lima and F. S. Lameiras, *Mater. Res. Bull.*, 2005, **40**, 1497.
103 T. Chattopadhyay, J. Pannetier and H. G. Von Schnering, *J. Phys. Chem. Solids*, 1986, **47**, 879.
104 J. M. Pietryga, R. D. Schaller, D. Werder, M. H. Stewart, V. I. Klimov and J. A. Hollingsworth, *J. Am. Chem. Soc.*, 2004, **126**, 11752.
105 M. V. Kovalenko, E. Kaufmann, D. Pachinger, J. Roither, M. Huber, J. Stangl, G. Hesser, F. Schaffler and W. Heiss, *J. Am. Chem. Soc.*, 2006, **128**, 3516.
106 J. R. Burke and H. R. Riedl, *Phys. Rev.*, 1969, **184**, 830.
107 B. A. Efimova, V. I. Kaidanov, B. Y. Moizhes and I. A. Chernik, *Sov. Phys. Solid State*, 1966, **7**, 2032.
108 M. V. Kovalenko, W. Heiss, E. V. Shevchenko, J. S. Lee, H. Schwinghammer, A. P. Alivisatos and D. V. Talapin, *J. Am. Chem. Soc.*, 2007, **129**, 11354.

109 H. Bonnemann, W. Brijoux and T. Joussen, *Angew. Chem., Int. Ed.*, 1990, **29**, 273.
110 V. I. Klimov, *J. Phys. Chem. B*, 2006, **110**, 16827.
111 J. J. Ning, K. K. Men, G. J. Xiao, B. Zou, L. Wang, Q. Q. Dai, B. B. Liu and G. T. Zou, *CrystEngComm*, 2010, **12**, 4275.
112 J. T. Hu, T. W. Odom and C. M. Lieber, *Acc. Chem. Res.*, 1999, **32**, 435.
113 J. H. Yu, J. Joo, H. M. Park, S. Baik, Y. W. Kim, S. C. Kim and T. Hyeon, *J. Am. Chem. Soc.*, 2005, **127**, 5662.
114 N. Pradhan, D. Reifsnyder, R. G. Xie, J. Aldana and X. Peng, *J. Am. Chem. Soc.*, 2007, **129**, 9500.
115 N. Kh. Abrikosov, V. F. Bankina, L. V. Poretskaya, L. E. Shelimova and E. V. Skudnova, *Semiconducting II–VI, IV–VI and V–VI Compounds*, Plenum Press, 1969.
116 A. Stanchev and C. Vodenicharov, *Thin Solid Films*, 1976, **38**, 67.
117 D. D. Vaughn, II, R. J. Patel, M. A. Hickner and R. E. Schaak, *J. Am. Chem. Soc.*, 2010, **132**, 15170.
118 D. V. Talapin, J. S. Lee, M. V. Kovalenko and E. V. Shevchenko, *Chem. Rev.*, 2010, **110**, 389.
119 A. Stavrinadis, J. M. Smith, C. A. Cattley, A. G. Cook, P. S. Grant and A. A. R. Watt, *Nanotechnology*, 2010, **21**, 185202.
120 Z. J. Wang, S. C. Qu, X. B. Zeng, J. P. Liu, C. S. Zhang, F. R. Tan, L. Jin and Z. G. Wang, *J. Alloys Compd.*, 2009, **482**, 203.
121 Z. J. Wang, S. C. Qu, X. B. Zeng, J. P. Liu, F. R. Tan, Y. Bi and Z. G. Wang, *Acta Mater.*, 2010, **58**, 4950.
122 Y. Wang, H. Gong, B. H. Fan and G. X. Hu, *J. Phys. Chem. C*, 2010, **114**, 3256.
123 R. O'Hayre, M. Nanu, J. Schoonman, A. Goossens, Q. Wang and M. Graetzel, *Adv. Funct. Mater.*, 2006, **16**, 1566.
124 D. B. Mitzi, M. Yuan, W. Liu, A. J. Kellock, S. J. Chey, V. Deline and A. G. Schrott, *Adv. Mater.*, 2008, **20**, 3657.
125 M. V. Kovalenko, M. I. Bodnarchuk, J. Zaumseil, J.-S. Lee and D. V. Talapin, *J. Am. Chem. Soc.*, 2010, **132**, 10085.